Chapter 5
Nanovisualization of Proteins in Action Using High-Speed AFM

Takayuki Uchihashi, Noriyuki Kodera, and Toshio Ando

5.1 Introduction

The dynamics of proteins, such as their conformational change and dynamic interplay with interaction partners, is crucial to their biological functions. To reveal the dynamic behavior of proteins, single-molecule approaches are indispensable because the molecules behave in an unsynchronized manner, which makes it difficult to monitor their dynamics by ensemble average experiments. Fluorescence microscopy has been widely used to study the functional behavior of single-protein molecules (Peterman et al. 2004; Joo et al. 2008; Roy et al. 2008; Yanagida and Ishii 2008). However, it only visualizes featureless fluorescent spots, meaning that protein molecules themselves are invisible. Moreover, what we can analyze using fluorescence techniques is limited to the behavior of a selected portion where a fluorophore is attached. Therefore, inferences have to be made to bridge the gap between the observed behavior of fluorescent spots and the actual behavior of labeled protein molecules. Consequently, it takes a considerably long time to reach a persuasive conclusion on how a protein dynamically behaves to function.

Atomic force microscopy (AFM) (Binnig et al. 1986) has made it possible for the first time to visualize the surface topography of samples at single-nanometer resolution even in liquid environments (Drake et al. 1989; Weisenhorn et al. 1989). In the early stage, pioneering studies explored this new capability by visualizing various biological samples under physiological conditions (Lindsay et al. 1989; Weisenhorn et al. 1989; Hansma et al. 1993; Schabert and Engel 1994; Müller et al. 1995; Shao

T. Uchihashi • T. Ando (✉)
Department of Physics and Bio-AFM Frontier Research Center, Kanazawa University, Kanawaza, Japan
e-mail: uchihast@staff.kanazawa-u.ac.jp; tando@staff.kanazawa-u.ac.jp

N. Kodera
Bio-AFM Frontier Research Center, Kanazawa University, Kanawaza, Japan
e-mail: nkodera@staff.kanazawa-u.ac.jp

119

and Yang 1995; Walz et al. 1996; Müller and Engel 1999). Moreover, several groups attempted to visualize dynamic biological processes (Bezanilla et al. 1994; Guthold et al. 1994; Kasas et al. 1997; Lin et al. 1999; Oberleithner et al. 2000). For example, the clotting process of fibrin (Drake et al. 1989), viral infection of isolated cells (Häberle et al. 1992), and antibody binding to an S-layer protein (Ohnesorge et al. 1992) were imaged at ~1 min or longer intervals. Therefore, in the early stage after the advent of AFM, researchers were already well aware that innovative biological studies would be opened by a new approach, i.e., visualization of dynamic events occurring with biological samples using AFM. In fact, one of the inventers of AFM, Gerd Binnig, mentioned as follows: "In biology, use of the force microscope will probably become quite common because of its ability to deliver films of processes" (Binnig 1992). However, we had to wait for this prediction to come true until 2008 when the instrumentation of high-speed AFM was completed.

Establishing both high-speed and low-invasive performances of AFM required lengthy efforts for solving various technical problems. In the early stage, small cantilevers (Schäffer et al., 1996; Ando et al. 2001), a fast scanner (Ando et al. 2001), a fast amplitude detector (Ando et al. 2001), and an optical beam deflection (OBD) sensor for detecting deflection of a small cantilever (Schäffer et al. 1996; Ando et al. 2001) were developed. Using HS-AFM equipped with some of these devices, fast imaging was attempted to visualize dynamic events of proteins (Vianni et al., 2000; Ando et al. 2001). However, it was evident that the bandwidth of feedback control to maintain the tip–sample interaction force constant was not high enough. Then, we further developed smaller cantilevers (Kitazawa et al. 2003; Ando et al. 2008), a faster z-scanner (Fukuma et al 2008), an active damping technique for the z-scanner (Kodera et al. 2005), a new proportional-integral-derivative (PID) feedback controller (Kodera et al. 2006), a compensator for drift in cantilever excitation efficiency (Kodera et al. 2006), and a fast amplitude detector with low noise performance (Ando et al. 2008).

Going through these developmental and proof-of-principle stages, HS-AFM has now moved to a new phase where we can use this microscopy to gain new insights into the functional mechanism of proteins. Various biomolecules and dynamic events have already been imaged by HS-AFM (Table 5.1). Although only imaged from the top direction, the whole topography of proteins and their minute temporal changes are visualized in some of these studies. Unlike fluorescence microscopy, various dynamic events of a molecule appear in the AFM movie without preselection, meaning that both expected and unexpected dynamic molecular behaviors can be visualized simultaneously. This gives a great chance of learning details of several facts of molecular dynamics in one imaging experiment. Moreover, the molecular dynamics that appears on video can often be interpreted quite easily without sophisticated analyses. These unique features of HS-AFM imaging significantly facilitate our understanding of the functional mechanism of proteins. In this chapter, we first briefly overview key technical developments in HS-AFM and then highlight our recent representative studies on dynamical properties of proteins. For other AFM imaging studies, see a recent review (Ando 2012).

Table 5.1 Summary of published high-speed AFM imaging studies

Subjects	Targets	References
Structure dynamics of proteins	Myosin V	Ando et al. (2001, 2002); Kodera et al. (2010)
	Dynein C	Ando et al. (2005)
	GroEL	Yokokawa et al. (2006a)
	Intrinsically disordered protein	Miyagi et al. (2008)
	$P2X_4$ receptor	Shinozaki et al. (2009)
	Bacteriorhodopsin	Shibata et al. (2010, 2011)
	Acid-sensing ion channel	Yokokawa et al. (2010)
	F_1-ATPase	Uchihashi et al. (2011)
Dynamic processes of proteins	Actin gliding	Ando et al. (2005)
	GroEL-ES	Ando et al. (2005); Yamamoto et al. (2009)
	Cellulase on cellulose	Igarashi et al. (2009, 2011)
	ClpX-FtzZ	Sugimoto et al. (2010)
	Amyloid-like fibrils	Milhiet et al. (2010)
	C-ring of F_0	Casuso et al. (2010)
Protein–DNA interactions	*ApaI* endnuclease-DNA	Yokokawa et al. (2006b)
	Type III restriction enzyme-DNA	Crampton et al. (2007)
	*EcoR*II restriction enzyme-DNA	Gilmore et al. (2009)
	Histone-nucleosome	Suzuki et al. (2010)
	Synthetic molecular transporter-DNA	Wickham et al. (2011)
Dynamics of 2D - protein crystals	Streptavidin	Yamamoto et al. (2008)
	Bacteriorhodopsin	Yamashita et al. (2009); Casuso et al (2009)
Dynamics of DNA	3D hollow structure of DNA origami	Endo and Sugiyama (2009); Endo et al. (2009)
	DNA origami jigsaw pieces	Endo et al. (2010a); Rajendran et al. (2011)
	DNA methylation	Endo et al. (2010b); Sannohe et al. (2010)
	G-quadruplex in DNA nanoscaffold	
	DNA cuboid	Endo et al. (2011)
Others	Process of cell death by antimicrobial peptide	Fantner et al. (2010)
	Lipid bilayer formation	Giocondi et al. (2010)
	Morphological transformation of detergent micelles	Inoue et al. (2011)

5.2 Overview of High-Speed-AFM Instrumentation

5.2.1 Overall Design of HS-AFM System

Among various operation modes of AFM, our HS-AFM system (Fig. 5.1) uses the tapping mode in which the cantilever tip is vertically oscillated at the first resonant frequency of the cantilever (Hansma et al. 1993; Zhong et al. 1993; Putman et al.
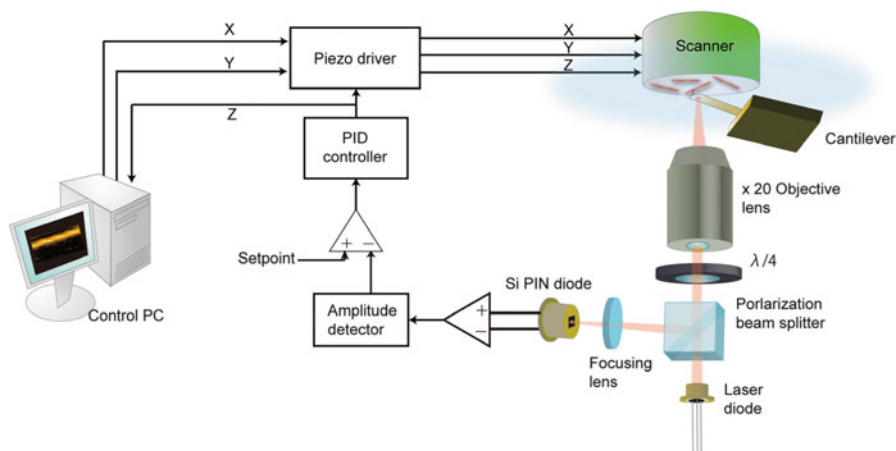
Fig. 5.1 Schematic of HS-AFM system

1994). The intermittent tip–sample contact eliminates the lateral force acting between tip and sample and thus prevents weakly adsorbed proteins from being dislodged from the substrate surface. Upon tip–sample contact, the cantilever oscillation amplitude decreases. During lateral scanning of the sample stage, the change in the amplitude is measured and then the sample stage is moved in the z-direction to recover the amplitude back to a given value (i.e., set point) through feedback control. For fast and nondestructive imaging of biological samples, the feedback control should be performed fast and precisely. Therefore, all devices contained in the feedback loop, i. e., the cantilever, the OBD sensor, the amplitude detector, the PID feedback circuit, the piezoactuator-based scanner, and the piezodriver, are optimized for their fast response.

The HS-AFM system includes an original inverted optical microscope. An objective lens with a long working distance used for the optical microscope is a part of the OBD sensor and is also used for viewing the cantilever and sample stage under the optical microscope, via a digital camera or a CCD camera. A glass slide, to which a cantilever holder and a liquid cell are attached, is placed on the optical microscope stage. A cantilever chip is held in the holder so that its tip points upwards (opposite to the way in conventional AFM). A sample stage attached to the z-scanner and facing downwards is placed over the cantilever. The instrument is now commercially available from the Research Institute of Biomolecule Metrology, Ltd. (Tsukuba, Japan).

5.2.2 Small Cantilevers and OBD Sensor

The cantilevers to be used in HS-AFM should have a high-resonant frequency and a small spring constant to meet both fast and low-invasive imaging capabilities, and

thus, they should be fabricated to a small size. We use small rectangular cantilevers, so-called beak-like cantilevers, made of silicon nitride (Kitazawa et al. 2003). The dimensions are ~6 μm long, ~2 μm wide, and ~90 nm thick (BL-AC7DS-KU5, custom-made by Olympus). They have resonant frequencies ~3.5 MHz in air and ~1.2 MHz in water, a spring constant ~0.2 N/m, and a quality factor ~2 in water. Slightly larger cantilevers (9–10 μm long, 2 μm wide, and 130 nm thick; BL-AC10DS, Olympus, Tokyo) with resonant frequencies 1.5 MHz in air and 0.6 MHz in water, a spring constant 0.1 N/m, and a quality factor $Q \sim 2$ in water are available from Olympus, Atomic Force F&E GmbH (Mannheim, Germany), Asylum Research (Santa Barbara, USA), and Bruker (Calle Tecate, USA). However, the apex of the beak-like tip is not small enough (25–100 nm) to acquire high-resolution images. We usually use electron-beam-deposited (EBD) tip grown on the original beak-like tip using a field emission scanning electron microscope (FE-SEM) (Wendel et al. 1995). As a sublimate for the EBD tip, phenol powder is used. A spot-mode electron beam is focused onto each original tip to produce a ~1 μm long needle composed of amorphous carbon at a growth rate of ~17 nm/s. The EBD tip is sharpened by oxygen or nitrogen plasma etching to an apex radius of ~4 nm (~0.5 nm at the best case).

In our OBD sensor (Ando et al. 2001), an incident laser beam is focused onto a small cantilever through a ×20 objective lens with a long working distance of 24 mm (Fig. 5.1). The light reflected back from the rear side of the cantilever is collected and collimated using the same objective lens and guided to a quadrant-cell Si PIN photodiode. The focused spot is 3–4 μm in diameter. The incident and reflected beams are separated using a quarter-wavelength plate and a polarization beam splitter. The small cantilevers provide the OBD sensor with high deflection detection sensitivity (10–20 times higher than conventional large cantilevers) because the angle change at the cantilever's free end is 10–20 times larger for a given vertical displacement of the tip.

5.2.3 Amplitude Detector and Feedback Controller

The oscillation amplitude of the cantilever should be detected as fast as possible with a high signal-to-noise ratio. A conventional RMS-to-DC converter and a lock-in amplifier require at least several oscillation cycles to output an accurate amplitude signal. We developed two types of fast amplitude detectors, a peak-hold type (Ando et al. 2001) and a Fourier type (Kokavecz et al. 2006; Ando et al. 2008). In the peak-hold analogue circuit, the peak and bottom voltages of the output signal from the OBD senor are held and their difference is output as an amplitude signal. The amplitude signal is renewed every half cycle of cantilever oscillation. In the Fourier type (analogue/digital hybrid system), Fourier cosine and sine coefficients (a_1, b_1) are calculated every one cycle of cantilever oscillation and a signal proportional to $(a_1^2 + b_1^2)^{1/2}$ is output. The Fourier method is less susceptible to cantilever's thermal fluctuations in the deflection than the peak-hold method.

For the feedback control under a small tapping force condition, the amplitude set point should be set close to the free oscillation amplitude of the cantilever. Under this condition, tip "parachuting" often occurs, and thus the error signal is saturated at a small value for a while. "Parachuting" means that the cantilever tip completely detaches from the sample surface at a steep down-hill region of the sample and time elapses until the tip lands on the surface again. To reduce or eliminate the parachuting time, we developed a dynamic PID controller in which the gain parameters are dynamically changed depending on the cantilever oscillation amplitude (Kodera et al. 2006). This dynamic PID controller can maintain the feedback bandwidth at a high level even when the amplitude set point is close to the cantilever free oscillation amplitude, making high-speed imaging compatible with low-invasive imaging. In addition, an electronics developed to compensate for the drift in the cantilever excitation efficiency allows stable imaging under the small tapping force condition (Kodera et al. 2006).

5.2.4   Scanner and Active Damping

We developed three types of scanners with different maximum scan ranges. Type-1: $x = 1$ μm, $y = 4$ μm, $z = 1$ μm; Type-2: $x = 5$ μm, $y = 5$ μm, $z = 2$ μm; and Type-3: $x = 40$ μm, $y = 40$ μm, $z = 6$ μm. Type-1 is used for dynamic imaging of isolated proteins, while the latter two types are used for dynamic imaging of larger objects such as bacteria and eukaryotic cells. Each type of scanner is composed of three piezoactuators that displace the sample along the x-, y-, and z-axes. The slowest y-scanner displaces a block of the x- and z-scanners, the x-scanner displaces a block of the z-scanner, and the z-scanner displaces a glass-rod sample stage. Each block is connected with the surrounding base through a pair of flexures to achieve small crosstalk between the three displacement axes (Ando et al. 2008). Since the x-piezo is sandwiched between two flexures, the center of mass of the x-piezo is unchanged, minimizing the impulsive force exerting to the surrounding base and thus minimizing the induction of vibrations. To counteract the impulsive force produced by the z-scanner displacement, two identical piezoactuators are attached to a supporting base and are displaced simultaneously with the same length in the opposite direction (Ando et al. 2001). For the fastest z-scanner with a first resonant frequency 370 kHz, a piezoactuator is held at the four rims parallel to the displacement direction in order to counteract the impulsive force (Fukuma et al. 2008).

The first resonant frequencies of the z-scanners are those of the actuators used, meaning that resonance arising from the designed structure occurs at higher frequencies. We developed an active damping technique to eliminate the resonant vibrations of the z-scanners using a new Q-controller with corresponding mock z-scanners composed of LRC circuits (Kodera et al. 2005).

5.2.5 Highest Possible Imaging Rate

As a consequence of the whole development described above, we have achieved the highest feedback bandwidth $f_B \sim 110$ kHz. This is at least 10 times higher than other nominal high-speed AFM instruments. The highest possible imaging rate R_{max} is a function of f_B, the scan range in the x-direction W, the number of scan lines N, the smallest sample surface corrugation to be observed λ, and the sample fragility (Ando et al. 2008; Ando 2012). The overall relationship can be expressed as

$$R_{max} = \frac{2\lambda f_B \theta_m}{\pi W N},$$ (5.1)

where θ_m represents an sample fragility-dependent allowable maximum phase delay in tracing the sample surface. Even for relatively fragile molecules ($\theta_m < \sim 20°$), we can capture images at 12 frames/s (fps) under the condition of $W = 200$ nm, $N = 100$, and $\lambda = 10$ nm without disturbing the physiological function of the molecules.

5.3 Imaging of Protein Molecules in Action

Some HS-AFM movies showing the dynamic behavior of proteins described below can be seen at http://www.s.kanazawa-u.ac.jp/phys/biophys/index.htm or at the corresponding publishers' homepages.

5.3.1 Myosin V

5.3.1.1 General Properties of Myosin V

Myosin V (M5) is a two-headed molecular motor that transports intracellular vesicles along actin filaments from the central regions of cells to the periphery (see a review; Sellers and Weisman 2008). Each N-terminal motor domain containing actin-binding and ATP hydrolysis sites is connected to an extended neck with six calmodulins (or five calmodulins and a light chain). The region containing the motor and neck domains is called "head." After the neck region, M5 is dimerized by a coiled-coil tail, which is followed by a C-terminal globular tail domain capable of binding to various cargos via adapter proteins (Fig. 5.2a). In order to elucidate the functional mechanism of M5, numerous studies have been done using biophysical and biochemical techniques. Using fluorescence microscopy and optical tweezers, it has been demonstrated that single molecules move processively along actin filaments towards the plus ends of the filaments (Mehta et al. 1999;
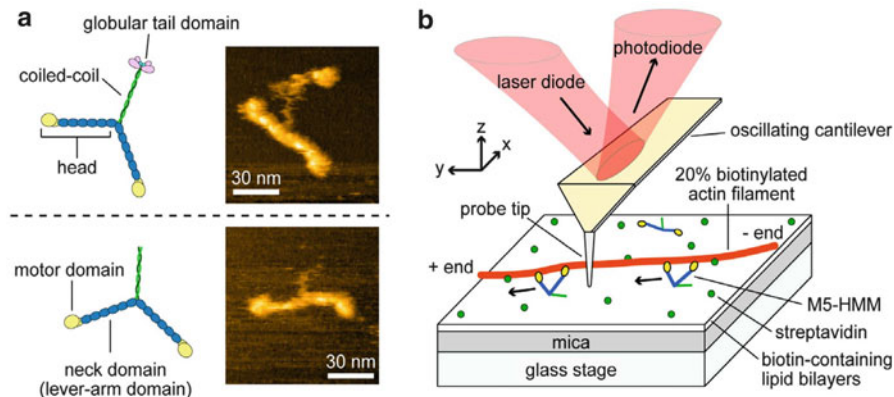
Fig. 5.2 (**a**) Schematic models and AFM images of M5 (*upper*) and M5-HMM (*lower*). (**b**) Schematic showing assay system for HS-AFM imaging of walking M5-HMM molecules

Sakamoto et al. 2000) in a hand-over-hand fashion (Forkey et al. 2003; Yildiz et al. 2003) with a 36-nm step for every ATP hydrolysis cycle (Sakamoto et al. 2008). Here, "hand-over-hand" means that the two heads alternate the leading and trailing positions at each step, very analogous to "walking." However, the protein molecules themselves are invisible in these studies and have therefore been visualized by electron microscopy only in the stationary states (Walker et al. 2000; Burgess et al. 2002; Oke et al. 2010). Thus, a comprehensive description of the molecule in action has not been accomplished until our recent HS-AFM study (Kodera et al. 2010). We briefly describe below some of our results.

5.3.1.2 Unidirectional Hand-Over-Hand Movement

As a substrate, we used a mica-supported lipid bilayer composed of an electrically natural phospholipid, a biotinylated phospholipid, and a positively charged phospholipid. The bilayer is in a gel phase at room temperature (Yamamoto et al. 2010). Partially biotinylated actin filaments were immobilized on the surface through streptavidin molecules with a low surface density (Fig. 5.2b). The positively charged lipid facilitated observing the characteristic sideways configuration of moving M5, allowing us to acquire high-resolution images. The successive AFM images captured at 7 fps in the presence of ATP (Fig. 5.3a) show M5-HMM (tail-truncated M5, bottom in Fig. 5.2a) moving processively along an actin filament with discrete ~36-nm steps. The two-headed bound M5-HMM showed unique structural features without exception, as illustrated in the bottom of Fig. 5.3a; the neck–motor domain junction appears smooth in the leading head whereas it is V-shaped in the trailing head, because the neck regions emerge from different parts of the motor domain. The short coiled-coil tail was mostly tilted towards the
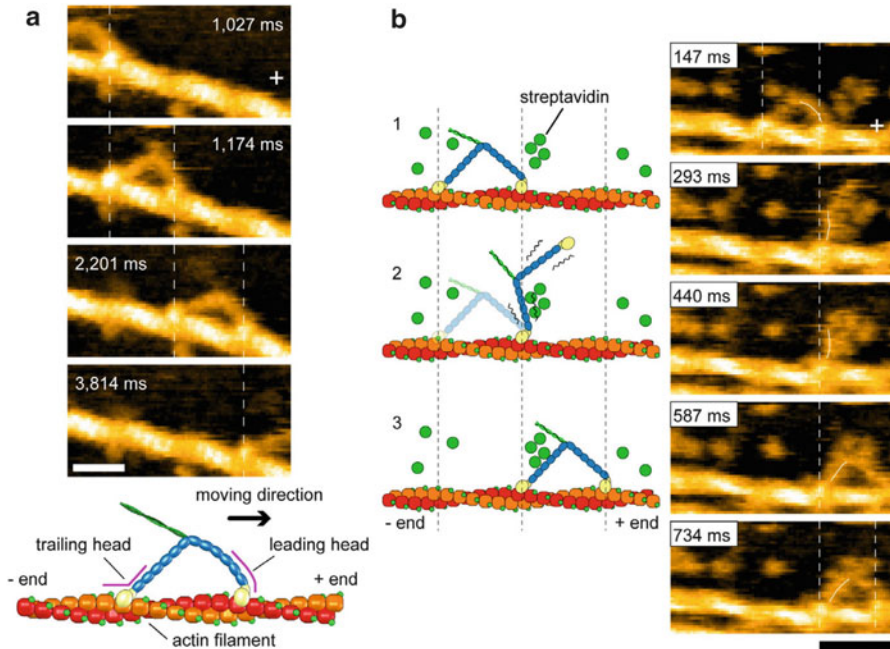
Fig. 5.3 (**a**) Successive AFM images showing unidirectional processive movement of M5-HMM observed in 1 μM ATP (*upper panels*; scale bar, 30 nm) and schematic showing two-headed bound M5-HMM (*bottom*). (**b**) Successive AFM images (*right panel*) showing hand-over-hand movement of M5-HMM in 1 μM ATP (scale bar, 50 nm) and schematic explaining the AFM images (*left panel*). The swinging lever is highlighted with the *thin white lines* (*right panel*). The *vertical dashed lines* in (**a**) and (**b**) show the *centers* of mass of the motor domains, and the *plus signs* indicate the plus ends of actin. All AFM images were taken at 7 fps

direction opposite to the moving direction. These features are totally consistent with those shown in electron micrographs (Walker et al. 2000) and can be used to determine the actin polarity when bound M5-HMM is stationary. However, the AFM movie could not resolve detailed stepping behaviors because the step completed within a frame.

To slow down the step motion, we additionally attached streptavidin molecules on the substrate surface as moderate obstacles to the movement, which successfully allowed us to directly visualize the detailed molecular processes during a step (Fig. 5.3b). After trailing head detachment from actin, the nearly straight leading head appeared to spontaneously swing from the reverse arrowhead orientation toward the arrowhead orientation, showing, for the first time, the swinging lever-arm motion initially proposed for muscle myosin (Huxley 1969). The detached trailing head rotationally diffused around the advancing neck–neck junction and then bound to a frontward actin site as a new leading head, completing one step. Thus, the detailed molecular behavior during hand-over-hand movement was directly visualized at unprecedented high spatiotemporal resolution. In the AFM movie, we did not observe

other behaviors of M5-HMM expected from the "inchworm" (Hua et al. 2002) model proposed for kinesin and the "biased diffusion" (Okada et al. 2007) model proposed for myosin, at least with the temporal resolution used.

5.3.1.3 Tension Generation and Foot Stomp

The seemingly spontaneous rotation of the leading head following trailing head detachment suggests that intramolecular tension for the advance has already existed in the two-headed bound molecule. In this bound state, the trailing head is in the arrowhead orientation. This orientation is a natural one at least for the ADP-bound and nucleotide-free myosin heads, and hence, the intramolecular tension is not produced by the bound trailing head. On the other hand, the leading head is not in the natural orientation (i.e., in the reverse arrowhead orientation) and hence pays energy cost to generate the intramolecular tension. In fact, the bound leading head is slightly curved outwards while the trailing head is straight (Fig. 5.3a). Upon trailing head detachment, the constraint keeping the bound leading head in the unnatural orientation is removed and hence the leading head spontaneously rotates forwards, meaning that the bound leading head is in the strained prestroke state and thus the lever arm swing is not accompanied by chemical transitions. This inferred view was reinforced by the observation that the short coiled-coil of two-headed bound M5-HMM was sometimes unfolded, and then the leading head rotated from the reverse arrowhead orientation to the arrowhead orientation (Fig. 5.4a), very much similar to the swinging lever arm motion observed as powerstroke in the hand-over-hand movement.

In general, during the actomyosin ATPase cycle, the strained prestroke state has been thought to be always formed through Pi release from an ADP-Pi bound head weakly interacting with actin (Goldman 1987; Geeves and Holmes 1999). Thus, it may be concluded that the strained prestroke state, which is formed directly by the binding of ADP-bound leading head to actin, does not participate in the forward step in ATP. However, we observed a molecular behavior in ATP that indicates that it does participate. In two-headed bound M5-HM, both of the motor domains frequently exhibited brief dissociation and reassociation on the same actin filament (or a brief translocation by around ± 5 nm along the actin filament), whereas M5-HMM remained at approximately the same position on the filament (Fig. 5.4b). We have termed this behavior "foot stomp." The briefly detached leading head does not carry bound Pi because Pi is already released from an ADP-Pi-bound M5 head immediately after its initial binding to actin (De La Cruz et al. 1999). Nevertheless, the detached leading head with only ADP bound rebinds to actin, still in the reverse arrowhead orientation, and then swings forward following trailing head detachment. The detachment of leading head during foot stomp is not caused by ATP binding to the leading head. As described below, a nucleotide-free leading head is often sharply bent. We never observed a sharply bent leading head before its foot stomp.
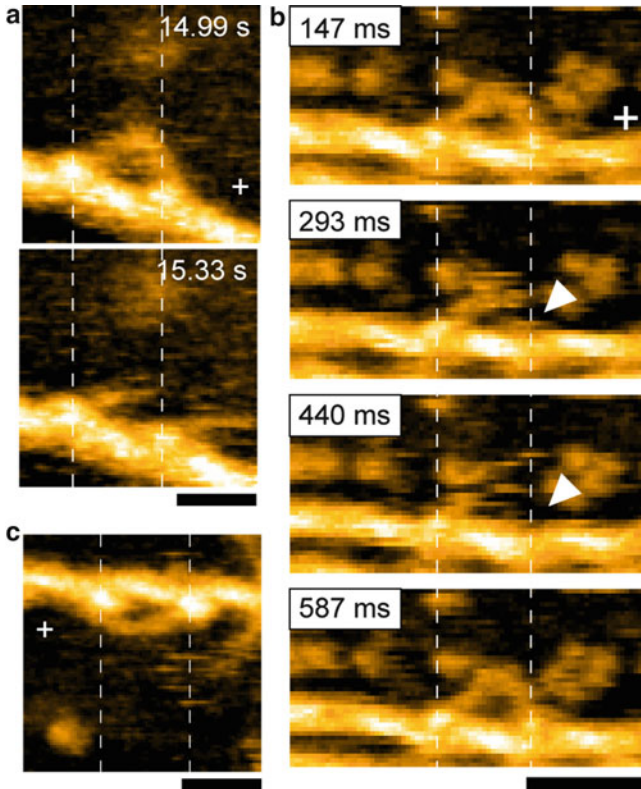
Fig. 5.4 Other dynamic events of M5 HMM observed by HS-AFM. (**a**) Unfolding of coiled-coil tail of two-headed bound M5-HMM in 50 μM ADP. *Top image*, before unfolding; *bottom image*, after unfolding. (**b**) Successive AFM images showing foot stomp at leading head observed in 1 μM ATP. The events of leading head detachment from actin are indicated with the *arrow heads*. Imaging rate, 7 fps. (**c**) AFM image showing sharply bent leading head of two-headed bound M5-HMM in the nucleotide free condition. The marks "*plus*" indicate the plus ends of actin filaments

5.3.1.4 Mechanism for Hand-Over-Hand Movement

The leading head of two-headed bound M5-HMM was always straight (slightly curved outwards) in ADP or ATP, while it was often sharply bent in the nucleotide-free condition (Fig. 5.4c). Therefore, just by looking at the conformation of leading head, we can judge whether or not the leading head contains nucleotides. To estimate the ADP dissociation rate constant at the leading head, M5-HMM bound to actin in various concentrations of ADP was observed, and then, the lifetime of straight leading head was analyzed as a function of ADP concentration. The ADP

dissociation rate constant at the leading head was estimated to be 0.1/s. This means that ADP is released from the leading head every 10 s, on average. However, M5-HMM walks many steps for 10 s, meaning that ADP does not dissociate from the leading head. That is, before ADP dissociation, the leading head is switched to the trailing head during walking. ADP dissociation, and the subsequent ATP binding, and the resulting detachment from actin solely occur at the trailing head. This is the basis underlying the processive hand-over-hand movement. This mechanism was inferred previously from various indirect experiments (Rosenfeld and Sweeney 2004; Purcell et al. 2005; Veigel et al. 2005; Forgacs et al. 2008; Oguchi et al. 2008; Sakamoto et al. 2008) but is now clearly observed by our high-speed AFM experiments. Moreover, we found that the foot stomps occurred more frequently at the leading head than at the trailing head. This asymmetry of foot stomp frequency between the two heads suggests that the leading head would be less susceptible to the catalytic activation by actin, which might contribute to some extent to the kinetic asymmetry between the two heads.

5.3.2 Rotary Catalysis of Rotorless F_1-ATPase

5.3.2.1 General Properties and Cooperativity of F_1-ATPase

ATP synthase, which is one of the most abundant proteins in organisms, synthesizes ATP from ADP and Pi using the electrochemical energy of proton gradient across membranes (Boyer 1993, 1997). It consists of two coupled rotary motors, called F_0 and F_1. F_0 is embedded in membranes while water-soluble F_1 is exposed to the solution. They can be separated and studied individually. F_1 is composed of five different subunits with a composition of $\alpha_3\beta_3\gamma\delta\epsilon$ (Todd et al. 1980; Walker et al. 1985). The three α and β subunits are arranged alternately to form a hexameric ring, and the central cavity of the hexamer is occupied by the γ subunit. The minimum rotary unit of F_1 is the $\alpha_3\beta_3\gamma$ subcomplex, in which the central γ shaft rotates within the $\alpha_3\beta_3$ stator ring when ATP is hydrolyzed by the ring (Matsui and Yoshida 1995). The catalytic site of F_1 is formed at the interface between the α and β subunits. The catalytic residues mainly reside in the β subunit (Abrahams et al. 1994). The rotational motion of γ has been demonstrated by single-molecule optical microscopy in which optical markers are attached to the γ subunit (Noji et al. 1997; Yasuda et al. 1998).

In the earliest obtained crystal structure (Fig. 5.5a), three catalytic sites are in different nucleotide-bound states; one binds to an ATP analog (β_{TP} and α_{TP}), another binds to ADP (β_{DP} and α_{DP}), and the third binds to none (β_E and α_E). Both β_{TP} and β_{DP} swing the C-terminal domain toward γ, assuming an inwardly retracted conformation, whereas β_E swings the domain away from γ, assuming an outwardly extended conformation. Because the two conformational states seem to push γ or be pushed by γ as shown in Fig. 5.5b and c, it was considered that the β–γ
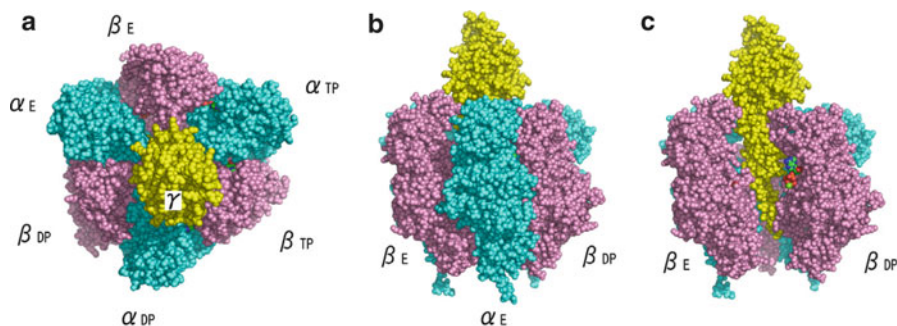
Fig. 5.5 Crystal structure of nucleotides-bound F_1-ATPase (PDB code: 1BMF). (**a**) *Top view*. (**b**) *Side view*. (**c**) *Side view* in which the α subunit on the nearest face is removed

interaction controls the conformational and catalytic states of individual β subunits and thus is essential for sequential torque generation (Wang and Oster 1998). Some biochemical studies are considered to suggest that the $\alpha_3\beta_3$ ring alone does not possess intrinsic cooperativity and γ mediates interplays among β's (Kaibara et al. 1996; Capaldi 1998; Nakamoto et al. 1999). On the other hand, although very few, there are biochemical studies that suggest that the intrinsic cooperativity is engendered by the $\alpha_3\beta_3$ ring alone (Yoshida and Allison 1990; Aloise et al. 1991).

Recently, it was reported that even when the interaction sites between β and γ are abolished, the γ still rotates unidirectionally (Hossain et al. 2006, 2008; Furuike et al. 2008). However, single-molecule optical microscopy does not allow us to directly examine whether the intrinsic cooperativity in the $\alpha_3\beta_3$ ring is responsible for sequential torque generation since attachment of a probe to the rotary shaft is required for visualization. We addressed this issue by directly imaging the ATP-driven conformational transition of β's in the isolated $\alpha_3\beta_3$ ring using high-speed AFM (Uchihashi et al. 2011).

5.3.2.2 AFM Observation of $\alpha_3\beta_3$ Subcomplex Without ATP

The $\alpha_3\beta_3$ subcomplex with Lys_7-tag at the N terminus of β was covalently immobilized on a mica surface treated first with 3-aminopropyl-triethoxysilane and then with glutaraldehyde. Therefore, the C-terminal domain of the $\alpha_3\beta_3$ subcomplex is at the top side. As shown in Fig. 5.6a, a ring structure with six high protrusions was observed under the nucleotide free conditions. Figure 5.6b shows an averaged high-resolution image of the $\alpha_3\beta_3$ subcomplex without nucleotide. This image shows a pseudo-sixfold symmetric ring in which three subunits alternately arranged in the ring are higher than the other three. The simulated AFM image of the C-terminal side of the ring constructed from the crystal structure of nucleotide-free $\alpha_3\beta_3$ subcomplex (Shirakihara et al. 1997) well reproduced the observed image
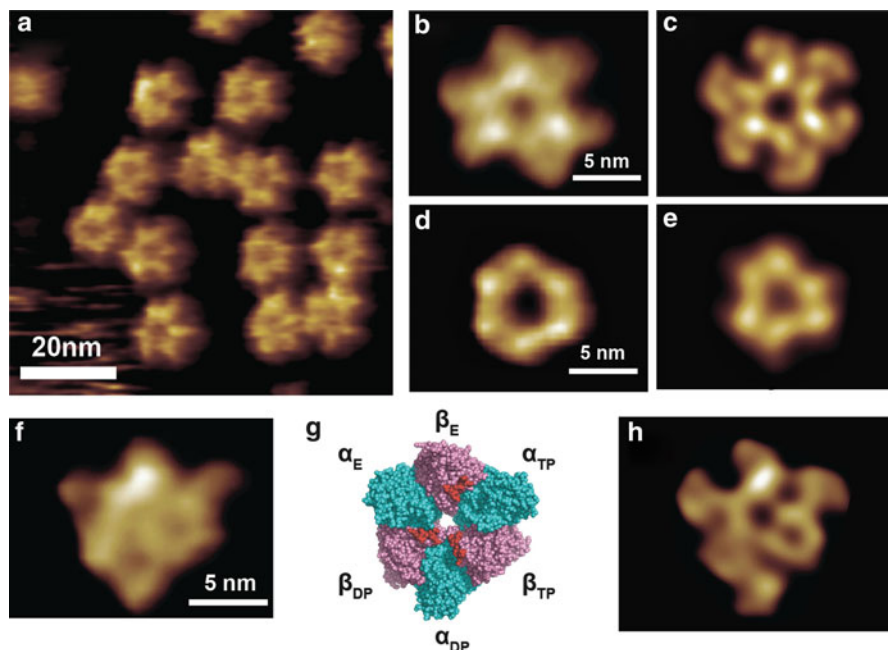
Fig. 5.6 (**a**) Wide-area AFM image of $\alpha_3\beta_3$ subcomplex without nucleotide. (**b**) and (**c**) are averaged experimental and simulated AFM images of C-terminal side of the $\alpha_3\beta_3$ subcomplex without nucleotide, respectively. (**d**) and (**e**) are averaged experimental and simulated AFM images of N-terminal side of the $\alpha_3\beta_3$ subcomplex without nucleotide. (**f**) Averaged AFM image of C-terminal side of the $\alpha_3\beta_3$ subcomplex in 1 mM AMPPNP. (**g**) Atomic structure of $\alpha_3\beta_3$ subcomplex with bound nucleotides. This structure is obtained by removing γ from a crystal structure of F_1. (**h**) Simulated AFM image constructed from the crystal structure shown in (**g**)

(Fig. 5.6c), indicating that the N-terminal side was in fact selectively attached to the mica, although a smaller crown corresponding to the N-terminal side was occasionally observed (Fig. 5.6d). The image was similar to a simulated image (Fig. 5.6e). Three β's, all assuming the outwardly extended conformation in the crystal structure of the $\alpha_3\beta_3$, gave three protrudent peaks in the simulated image as bright spots, and thus the three subunits showing higher protrusions seen in the AFM image were identified as β's.

When AMPPNP, which is a nonhydrolyzable ATP analog, was added, the ring became triangular and the central hole was obscure as shown in Fig. 5.6f. Three α's having the lower protrusions retained the same conformation as those under the nucleotide-free condition and two of the three β's retracted towards the center and at the same time lowered their protrusions. This structure did not change during the observation. A simulated image of $\alpha_3\beta_3$ with bound nucleotides (Fig. 5.6h), which was constructed using the crystal structure (Abrahams et al. 1994) of F_1 without γ (Fig. 5.6g), showed an asymmetric ring very similar to the observed image.

This excellent agreement indicates that only two β's can assume the inwardly retracted conformation even in saturating AMPPNP, which is consistent with the previous observation that three β's do not assume the inwardly retracted conformation simultaneously (Menz et al. 2001).

5.3.2.3   HS-AFM Observation of $\alpha_3\beta_3$ Subcomplex in ATP

In the presence of ATP, the ring shape was very similar to that observed in the presence of AMPPNP but the ring showed distinct conformational dynamics; each β underwent conformational transition between the outwardly extended high state (O-state) and the retracted low state (C-state) (Fig. 5.7a); the outwardly extended and inwardly retracted conformations are well correlated with the high and low protrusion states, respectively (Fig. 5.7b). Prominent features observed are that when the O-to-C transition occurs at one β, the opposite C-to-O transition occurs simultaneously at its counterclockwise neighbor β in most cases as shown in Fig. 5.7a. By this cooperative effect, the CCO conformational state propagates in the counterclockwise direction as seen in the time evolution of the cumulated angle of the open-β position relative to the center of the ring (Fig. 5.7c).

The rate of rotational propagation of the CCO conformational state increased with increasing ATP concentration (2–4 μM), indicating that ATP binding is rate limiting. The rate constant of the counterclockwise O-to-C shift in β at each ATP concentration was comparable with the corresponding initial rate of ATP hydrolysis measured biochemically. Thus, ATP hydrolysis is well coupled with the O-to-C transition of β.

The interplay between β subunits in $\alpha_3\beta_3$ responsible for the rotational propagation of the CCO conformational state was further supported by the following observation. A single subunit was occasionally dissociated from $\alpha_3\beta_3$ during observation (Fig. 5.7d), due presumably to the imperfect covalent binding of the subcomplex to the mica surface and to transient strong tip–sample interaction. Once one β is lost, the rotary propagation completely ceased (Fig. 5.7e), although some cooperative conformational transitions occurred between the remaining β's.

These results provide clear evidence that the structural basis of unidirectional rotary catalysis is intrinsically programmed in the stator ring. Thus, the "γ-dictator" model (Furuike et al. 2008), which proposes that only the interaction with γ determines the conformational and catalytic states of β's (Adachi et al. 2007; Watanabe et al. 2010), does not seem to be valid. On the other hand, the ATP-binding rate and the efficiency of unidirectionality of the CCO state propagation are distinctly lower than those of F_1 (Uchihashi et al. 2011). Thus, the interaction with γ is dispensable but still important for the rapid and precise rotary catalysis. Our findings are not inconsistent with the observations that the rate of the catalytic reaction are apparently under the control of the rotary angle of γ (Itoh et al. 2004; Rondelez et al. 2005; Iko et al. 2009). The intrinsic interplay among β's would reinforce the catalytic control by γ; even if γ tightly interacts with only one β, it still can act on all β's through β–β interplay.
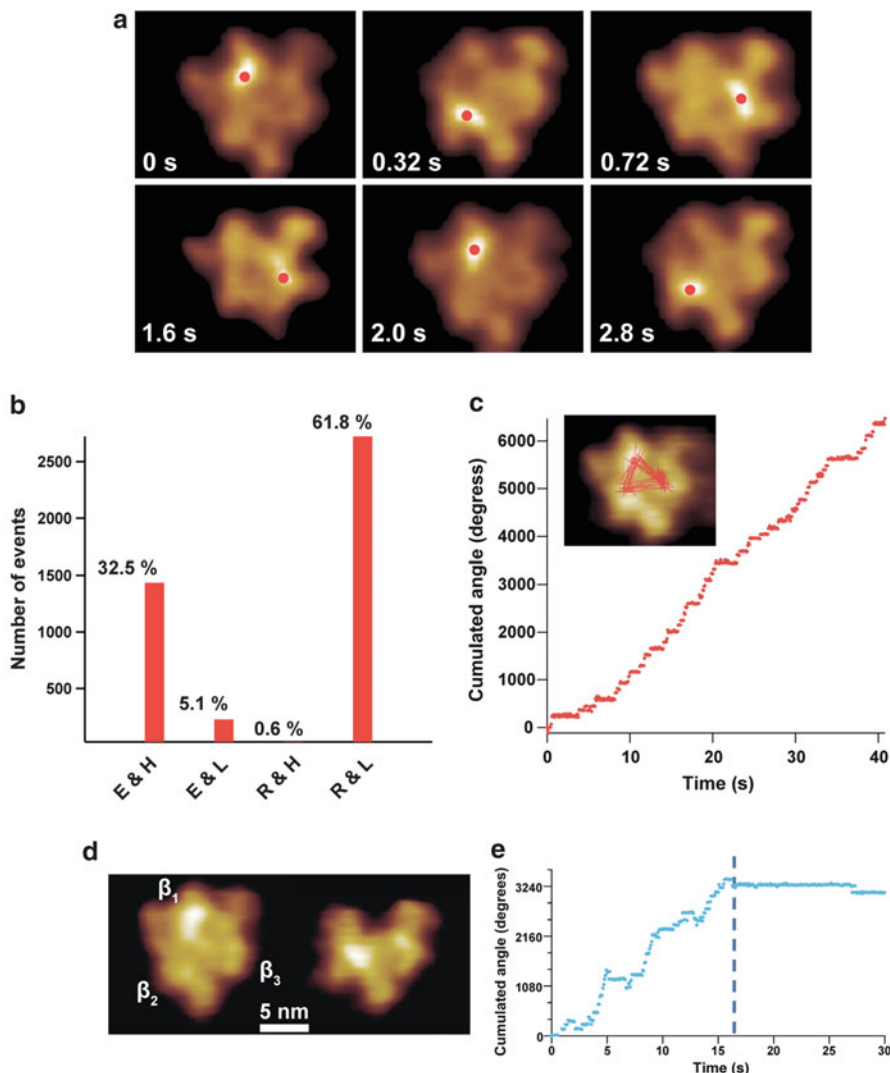
Fig. 5.7 (**a**) Successive AFM images showing conformational change in $\alpha_3\beta_3$ subcomplex in 2 μM ATP. The highest pixel in each image is indicated by the *red circle*. Frame rate, 12.5 fps. (**b**) Tight correlation between two types of conformational changes in β observed in ATP; conformations with different-height protrusions ("H," high; "L," low) and outwardly extended (E) and inwardly retracted (R) conformations of the distal region. The higher protrusion is mostly accompanied by the E-conformation, whereas the lower protrusion is mostly accompanied by the R-conformation. (**c**) Time evolution of cumulated angle of highest pixel. The inset shows a trajectory, superimposed on an AFM image, of the highest pixels corresponding to the high protrusions of β's. The center of rotation is defined by the averaged *x*- and *y*-positions of the highest pixels, and the cumulated angles are calculated relative to the first frame. (**d**) and (**e**) Cessation of rotary propagation of conformational states upon loss of a single subunit. (**d**) AFM images before (*left*) and after (*right*) loss of β_1. (**e**) Cumulated angles of open β measured using the highest pixel position in each frame. ATP concentration, 2 μM; frame rate, 12.5 fps. β_1 is lost at 16.2 s

5.3.3 Processive Movement and Traffic Jams of Cellulase on Cellulose Surface

5.3.3.1 General Issues of Cellulose Hydrolysis by Cellulase

Cellulase, which is produced mainly by cellulolytic fungi and bacteria, is a group of enzymes that degrade the plant polysaccharide called cellulose, a linear polymer connected by β-1,4 linkages (Ryu and Mandels 1980; Hon 1994). Although all types of cellulases can hydrolyze amorphous cellulose, only a limited number of cellulases can hydrolyze crystalline cellulose (Teeri 1997). The enzymes that hydrolyze crystalline cellulose are called cellobiohydrolases (CBHs) because the major product of the reaction is cellobiose, a soluble β-1,4-glucosidic dimer (Teeri et al. 1998). CBHs share a similar two-domain structure consisting of a catalytic domain (CD) and a cellulose-binding domain (CBD) (Abuja et al. 1988a, b, 1989). The two domains are connected by a highly O-glycosylated linker region (Rouvinen et al. 1990; Divne et al. 1994, 1998). At the initial step of the reaction, the cellulase enzymes adsorb onto the surface of crystalline cellulose via the CBD, and then glucosidic linkages are hydrolyzed by the CD (Johansson et al. 1989; Ståhlberg et al. 1991). Loss of the CBD causes a significant decrease in crystalline cellulose degradation but has less effect on the hydrolysis of soluble or amorphous cellulose, suggesting that adsorption of the enzymes on the surface via the CBD is essential for the effective hydrolysis of crystalline cellulose (Ståhlberg et al. 1991). The CD has a relatively long tunnel formed by surface loops with catalytic amino acids extending from the central fold of the CD. A cellulose chain threads through the tunnel and is hydrolyzed (Divne et al. 1994, 1998). Therefore, it has been considered that CBHs hydrolyze crystalline cellulose chains in a processive manner, making consecutive cuts without releasing the chain (Davies and Henrissat 1995; Reverbel-Leroy et al. 1997), but this idea has not been experimentally verified until recent HS-AFM imaging studies (Igarashi et al. 2009, 2011). The CBHs are categorized into two main types; CBH I hydrolyzes cellulose from the reducing end of cellulose, while CBH II does from the nonreducing end (Henrissat and Bairoch 1993). The CD of CBH I belongs to the glycoside hydrolase (GH) family 7 and the CD of CBH II belongs to the GH family 6.

Although the kinetics of crystalline cellulose hydrolysis by CBHs has been investigated extensively, the mechanism of crystalline cellulose degradation by CBHs is still elusive. For example, although it is known that the hydrolysis rate decreases rapidly with time (Eriksson et al. 2002), its mechanism is not fully understood. Furthermore, several studies indicate that CBH I and CBH II types display strong synergy for the hydrolysis of cellulose (Henrissat et al. 1985; Boisset et al. 2000), but the reason for the synergy effect is not yet revealed. The main reason for the difficulty in understanding these issues is the lack of analytical methods to monitor the enzymatic reaction at the solid/liquid interface.

5.3.3.2   Processive Run of Cellulase on Cellulose I$_\alpha$

The dynamic behavior of CBHs on a crystalline cellulose substrate was visualized using HS-AFM (Igarashi et al. 2009, 2011). We first observed a CBH I (*Tr*Cel7A) secreted from the industrially important cellulolytic ascomycete fungus *Trichoderma reesei*. *Tr*Cel7A is one of the best-studied CBHs (Abuja et al. 1989; Henrissat 1991; Henrissat and Bairoch 1993; Divne et al. 1994; Linder 1997; Henrissat et al. 1998; Boraston et al. 2004). We used a crystalline cellulose prepared from the cell wall of green algae, which consists of mainly cellulose I$_\alpha$ (Hon 1994). As a substrate surface, we chose highly ordered pyrolytic graphite (HOPG) because its hydrophobic surface has a high affinity for the hydrophobic surface of the crystalline cellulose. Figure 5.8a shows HS-AFM images of *Tr*Cel7A molecules moving unidirectionally and processively on the cellulose I$_\alpha$ surface. This movement of *Tr*Cel7A was observed only on the top surface of the cellulose crystal where the individual molecules were moving in a line. Interestingly, as shown in Fig. 5.8b, the movement of molecules was often halted due probably to the presence of an obstruction on the crystalline cellulose surface. When the movement of a molecule was halted, the following molecules were blocked and/or slowed down (Igarashi et al. 2011). These phenomena resemble the movement of traffic on a road.

   To evaluate the velocity of the movement, we tracked the center of each molecule. Figure 5.8c shows the time courses of displacement for seven molecules. Some molecules move continuously without stopping, whereas the movement of some molecules was occasionally halted or slowed down (the open green and closed red plots in Fig. 5.8c). Figure 5.8d shows a histogram of the measured velocity values. The histogram comprises two Gaussian distributions of the average velocity with mean $\pm$ SD values of -0.32 ± 3.4 and 7.1 ± 3.9 nm/s. This is consistent with the idea that *Tr*Cel7A has two modes of adsorption on a cellulose surface; the productive adsorption mode in which both CD and CBD contribute to the binding and the nonproductive adsorption mode in which the enzyme binds only via the CBD (Ståhlberg et al. 1991). The overall average velocity for many molecules was 5.3 ± 4.9 nm/s. From the velocity, the hydrolysis rate is estimated to be 5/s taking into account that one hydrolysis drives the movement of the molecule by 1 nm, which is the length of cellobiose. Surprisingly, this value is 500 times larger than that (0.01/s) estimated biochemically (Nidetzky et al. 1994). This inconsistency is presumably because in the biochemical estimation of the hydrolysis rate, it is assumed that all molecules productively work on the cellulose surface. However, the number of reduced ends available for *Tr*Cel7A binding is limited and the movement of many molecules is hampered by the traffic jams.

5.3.3.3   Processive Run of Cellulase on Cellulose III$_\text{I}$

The fabric form of cellulose I$_\alpha$ can be converted to cellulose III$_\text{I}$ polymorph by supercritical ammonia treatment (Igarashi et al. 2007). Although it is known that this conversion dramatically enhances the cellulose hydrolysis by *Tr*Cel7A
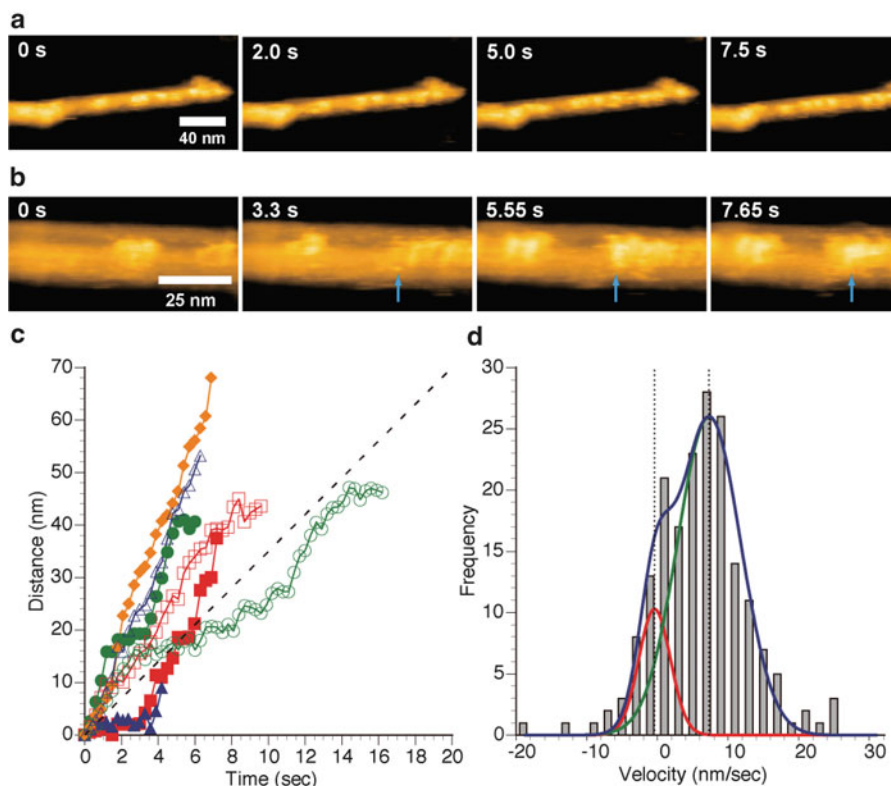
Fig. 5.8 Successive AFM images showing processive and unidirectional movement of *Tr*Cel7A on crystalline cellulose I_α (**a**, **b**). Frame rate, 1.1 fps. (**a**) The enzyme molecules move from the *right* to *left* on the crystal. (**b**) The movement of one molecule is halted and then following molecules are blocked at a position indicated by *arrows*. (**c**) Time course of displacement for individual *Tr*Cel7A molecules. The *different symbols* indicate different molecules. (**d**) Velocity distribution of linearly moving *Tr*Cel7A molecules on crystalline cellulose I_α. The histogram was fitted by the combination (*blue line*) of two Gaussian distribution curves with mean $\pm$ SD values of -0.32 ± 3.4 (*red*) and 7.1 ± 3.9 (*green*)

(Igarashi et al. 2007), its mechanism is unknown. We investigated this issue by visualizing the degradation of cellulose III_I (Igarashi et al. 2011). Figure 5.9a shows successive images of *Tr*Cel7A molecules processively moving on a cellulose III_I surface. The number of molecules on the cellulose III_I surface appears larger than that on the cellulose I_α surface shown in Fig. 5.9a although the velocity of the molecules on both surfaces is similar. In the case of cellulose I_α, the molecules only slide along limited lanes, whereas on cellulose III_I *Tr*Cel7A molecules moved over almost the whole exposed surface. This is due probably to the difference of affinity for *Tr*Cel7A between cellulose I_α and III_I. Comparing the crystalline shapes of cellulose I_α and III_I (Nishiyama et al. 2003; Wada et al. 2004), cellulose I_α has a hydrophobic surface (where the enzyme molecule can bind) at (110) surface (Fig. 5.9c), whereas cellulose III_I has a hydrophobic surface not only at (110)
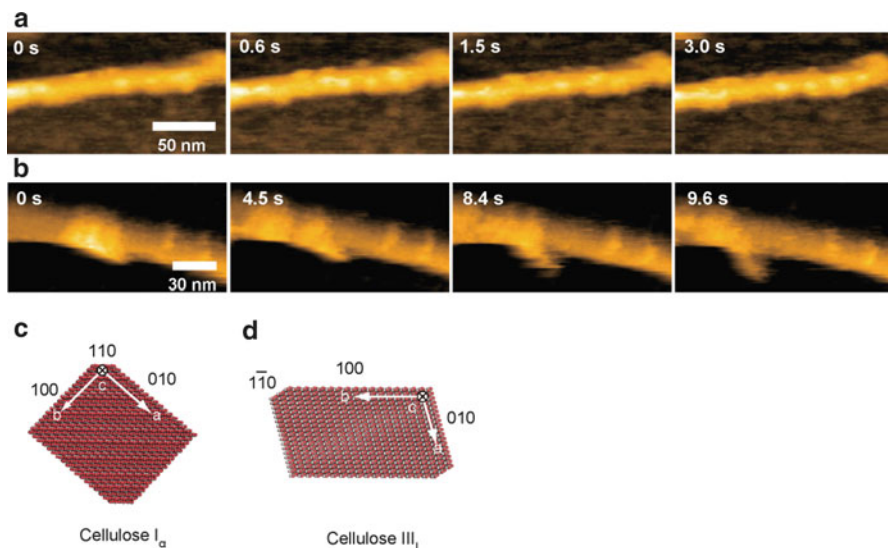
Fig. 5.9 (**a**) Successive AFM images of *Tr*Cel7A molecules on crystalline cellulose III$_I$. Frame rate, 3.3 fps. (**b**) Fibrillation of crystalline cellulose III$_I$ after congestion of molecules. Frame rate, 3.3 fps. Schematics of sections of crystalline cellulose I$_\alpha$ (**c**) and cellulose III$_I$ (**d**)

surface but also at (100) surface as shown in Fig. 5.9d. Therefore, cellulose III$_I$ has more lanes available for cellulase movement and thus causes less traffic jams. This is the mechanism underlying the enhanced degradation of cellulose III$_I$.

The traffic jams occurring on cellulose III$_I$ showed a unique feature that did now appear on cellulose I$_\alpha$. After several additional molecules were blocked, the enzyme molecules started to move again on the surface and at the same time a cellulose bundle was peeled off from the crystalline cellulose as shown in Fig. 5.9b. This phenomenon suggests that one enzyme molecule is unable to overcome an obstacle to the advance but accumulation of molecules behind the blocked molecule overcomes the obstacle. As a result, the blocked molecules restart linear movement from the point where the first molecule had stopped.

5.3.3.4 Synergetic Hydrolysis by *Tr*Cel7A and *Tr*Cel6A

As shown in Fig. 5.10a, two major CBHs, *Tr*Cel7A and *Tr*Cel6A, synergistically increase the efficiency of cellulose III$_I$ hydrolysis. This effect has been called exo-exo synergy (Nidetzky et al. 1994). Previous transmission electron microscopic observations of a crystalline cellulose after partial hydrolysis by both *Tr*Cel6A and *Tr*Cel7A showed that the two enzymes degrade the cellulose from different ends of the crystal; *Tr*Cel7A degrades the crystal from the reducing end, leading to fibrillation, thinning of the crystal, or narrowing of the crystal end, whereas *Tr*Cel6A
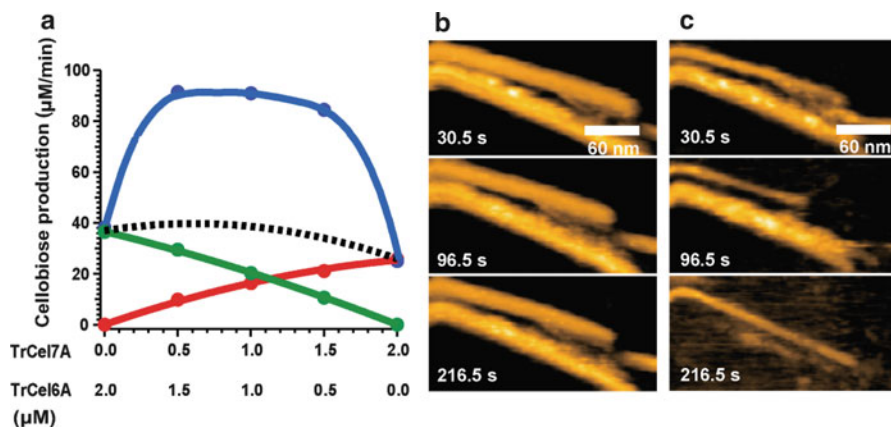
Fig. 5.10 (**a**) Synergy between *Tr*Cel6A and *Tr*Cel7A in cellobiose production from cellulose III$_I$. The *green* and *red plots* show the rates of cellobiose production by *Tr*Cel6A and *Tr*Cel7A, respectively, and the *blue plot* shows the synergy between the two enzymes. The *dotted line* indicates the simple sum of cellobiose production calculated from the *green* and *red plots*. (**b**) Successive AFM images after injection of *Tr*Cel6A to cellulose III$_I$ at 0 s. The cellulose was not degraded even at 8 min. (**c**) Successive AFM images after *Tr*Cel7A was additionally added at 0 s (at 8.4 min after the initial addition of *Tr*Cel6A). The cellulose was rapidly degraded and almost disappeared at ~4 min. Frame rate, 3.3 fps for (**b**) and (**c**)

hydrolyzes the crystal from the nonreducing end, less processively than *Tr*Cel7A, thereby sharpening the crystal tip (Chanzy and Henrissat 1985; Imai et al. 1998). It is however difficult to explain this type of synergistic action based on their exoenzymatic activity. We imaged the hydrolytic process with crystalline cellulose III$_I$ in the presence of both *Tr*Cel6A and *Tr*Cel7A to understand the mechanism underlying the synergetic degradation (Igarashi et al. 2011).

Cellulose III$_I$ was first imaged in the presence of *Tr*Cel6A alone. The appearance of the cellulose crystals did not significantly change during incubation over ~8 min, even though many enzyme molecules were observed on the cellulose surfaces (Fig. 5.10b). After *Tr*Cel7A was additionally added, enzyme molecules started moving from many points on the cellulose surfaces, and the degradation of crystalline cellulose was dramatically faster than the case with *Tr*Cel7A alone as shown in Fig. 5.10c. Eventually, the cellulose crystals almost disappeared at ~4 min after the addition of *Tr*Cel7A. The observed synergy was independent of the order of addition of *Tr*Cel6A and *Tr*Cel7A. A very similar synergy effect was also observed when both *Tr*Cel6A and *Tr*Cel7A were added simultaneously. These results suggest that *Tr*Cel6A is also an endoenzyme and the synergy observed is therefore endo–exo synergy (Wood and McCrae 1978), although *Tr*Cel6A is generally defined as an exo-glucanase (cellobiohydrolase). If so, *Tr*Cel6A generates nicks in the middle of crystalline cellulose, and these nicks become starting and ending points for *Tr*Cel7A activity.

The present results provide us with some clues to improving the efficiency of conversion from crystalline cellulose to cellobiose by cellulase enzymes. The following strategies should improve the conversion efficiency: flattening the surface of crystalline cellulose to remove obstacles to the advance of the enzymes; increasing the number of lanes by means of pretreatment of cellulose; combining exo- and endo-cellulase enzymes to increase the number of entrances and exits for the exoenzymes.

5.4 Concluding Remarks

In this chapter, we demonstrate that HS-AFM has been developed to the stage where it can be used to directly visualize dynamic processes and structure dynamics of proteins and other biological molecules with unprecedented temporal and spatial resolution. This capability allows us to visually and directly understand how biomolecules operate and function. As demonstrated by our recent results highlighted in this chapter, HS-AFM can provide unique new insights into the functional mechanism of proteins unattainable with previous single-molecule techniques.

Other than the examples describe here, our HS-AFM instrument has already been applied to studying dynamics of various proteins and macromolecular assemblies (Table 5.1); for instances, alternate binding of GroES to the two rings of GroEL (Yamamoto et al. 2009), dynamics of protein 2D crystals (Yamamoto et al. 2008; Yamashita et al. 2009), wiggling motion of intrinsically disordered regions of FACT protein (Miyagi et al. 2008), and photoinduced conformational change of bacteriorhodopsin (Shibata et al. 2010, 2011). Our HS-AFM apparatus is now commercialized by RIBM (Tsukuba, Japan) and has found many other applications (Yokokawa et al. 2006a, b; Crampton et al. 2007; Shinozaki et al. 2009; Casuso et al. 2010; Milhiet et al. 2010; Sugimoto et al. 2010; Wickham et al. 2011). The application of this new type of microscopy is now expanding and should become a tool commonly used for biophysical studies in the near future.

References

Abrahams JP, Leslie AGW, Lutter R, Walker JE (1994) Structure at 2.8 Å resolution of F1-ATPase from bovine heart mitochondri. Nature 370:621–628

Abuja PM, Pilz I, Claeyssens M, Tomme P (1988a) Domain structure of cellobiohydrolase II as studied by small angle X-ray scattering: close resemblance to cellobiohydrolase I. Biochem Biophys Res Commun 156:180–185

Abuja PM, Schmuck M, Pilz I, Tomme P, Claeyssens M, Esterbauer H (1988b) Structural and functional domains of cellobiohydrolase I from trichoderma reesei. Eur Biophys J 15:339–342

Abuja PM, Pilz I, Tomme P, Claeyssens M (1989) Structural changes in cellobiohydrolase I upon binding of a macromolecular ligand as evident by SAXS investigations. Biochem Biophys Res Commun 165:615–623

Adachi K, Oiwa K, Nishizaka T, Furuike S, Noji H, Itoh H, Yoshida M, Kinosita K (2007) Coupling of rotation and catalysis in F_1-ATPase revealed by single-molecule imaging and manipulation. Cell 130:309–321

Aloise P, Kagawa Y, Coleman PS (1991) Comparative Mg^{2+}-dependent sequential covalent binding stoichiometries of 3'-O-(4-benzoyl)benzoyl adenosine 5'-diphosphate of MF_1, TF_1, and the alpha 3 beta 3 core complex of TF_1. The binding change motif is independent of the F1 gamma delta epsilon sub. J Biol Chem 266:10368–10376

Ando T (2012) High-speed atomic force microscopy coming of age. Nanotechnology 23:062001 (27 pp)

Ando T, Kodera N, Maruyama D, Takai E, Saito K, Toda A (2002) A high-speed atomic force microscope for studying biological macromolecules in action. Jpn J Appl Phys 41:4851–4856

Ando T, Kodera N, Takai E, Maruyama D, Saito K, Toda A (2001) A high-speed atomic force microscope for studying biological macromolecules in action. Proc Natl Acad Sci USA 98:12468–12472

Ando T, Kodera N, Uchihashi T, Miyagi A, Nakakita R, Namashita H, Matada K (2005) High-speed atomic force microscopy for capturing dynamic behavior of protein molecules at work. e-J Surf Sci Nanotech 3:384–392

Ando T, Uchihashi T, Fukuma T (2008) High-speed atomic force microscopy for nano-visualization of dynamic biomolecular processes. Prog Surf Sci 83:337–437

Bezanilla M, Drake B, Nudler E, Kashlev M, Hansma PK, Hansma HG (1994) Motion and enzymatic degradation of DNA in the atomic force microscope. Biophys J 67:2454–2459

Binnig G (1992) Force microscopy. Ultramicroscopy 42–44:7–15

Binnig G, Quate C, Gerber C (1986) Phys Rev Lett 56:930–933

Boisset C, Fraschini C, Schulein M, Henrissat B, Chanzy H (2000) Imaging the enzymatic digestion of bacterial cellulose ribbons reveals the endo character of the cellobiohydrolase Cel6A from humicola insolens and its mode of synergy with cellobiohydrolase Cel7A. Appl Environ Microbiol 66:1444–1452

Boraston AB, Bolam DN, Gilbert HJ, Davies GJ (2004) Carbohydrate-binding modules: fine-tuning polysaccharide recognition. Biochem J 382:769–781

Boyer PD (1993) The binding change mechanism for ATP synthase–some probabilities and possibilities. Biochim Biophys Acta 1140:215–250

Boyer PD (1997) The ATP synthase–a splendid molecular machine. Annu Rev Biochem 66:717–749

Burgess S, Walker M, Wang F, Sellers JR, White HD, Knight PJ, Trinick J (2002) The prepower stroke conformation of myosin V. J Cell Biol 159:983–991

Capaldi RA (1998) Unisite Catalysis without Rotation of the γ - ε Domain in *Escherichia coli* F_1-ATPase. Biochemistry 273:15940–15945

Casuso I, Kodera N, Le Grimellec C, Ando T, Scheuring S (2009) High-resolution high-speed contact mode atomic force microscopy movies of purple membrane. Biophys J 97:1354–1361

Casuso I, Sens P, Rico F, Scheuring S (2010) Experimental evidence for membrane-mediated protein-protein interaction. Biophys J 99:L47–L49

Chanzy H, Henrissat B (1985) Unidirectional degradation of Valonia cellulose microcrystals subjected to cellulase action. FEBS Lett 184:285–288

Crampton N, Yokokawa M, Dryden DTF, Edwardson JM, Rao DN, Takeyasu K, Yoshimura SH, Henderson RM (2007) Fast-scan atomic force microscopy reveals that the type III restriction enzyme EcoP15I is capable of DNA translocation and looping. Proc Natl Acad Sci USA 104:12755–12760

Davies G, Henrissat B (1995) Structures and mechanisms of glycosyl hydrolases. Structure 3:853–859

Divne C, Stahlberg J, Reinikainen T, Ruohonen L, Pettersson G, Knowles J, Teeri T, Jones T (1994) The three-dimensional crystal structure of the catalytic core of cellobiohydrolase I from Trichoderma reesei. Science 265:524–528

Divne C, Ståhlberg J, Teeri TT, Jones TA (1998) High-resolution crystal structures reveal how a cellulose chain is bound in the 50 A long tunnel of cellobiohydrolase I from Trichoderma reesei. J Mol Biol 275:309–325

Drake B, Prater C, Weisenhorn A, Gould S, Albrecht T, Quate C, Cannell D, Hansma H, Hansma P (1989) Imaging crystals, polymers, and processes in water with the atomic force microscope. Science 243:1586–1589

Endo M, Sugiyama H (2009) Three-dimensional DNA nanostructures constructed by folding of multiple rectangles. Nucleic Acids Symp Ser 53:81–82

Endo M, Hidaka K, Kato T, Namba K, Sugiyama H (2009) DNA prism structures constructed by folding of multiple rectangular arms. J Am Chem Soc 131:15570–15571

Endo M, Hidaka K, Sugiyama H (2011) Direct AFM observation of an opening event of a DNA cuboid constructed via a prism structure. Org Biomol Chem 9:2075–2077

Endo M, Katsuda Y, Hidaka K, Sugiyama H (2010a) Regulation of DNA methylation using different tensions of double strands constructed in a defined DNA nanostructure. J Am Chem Soc 132:1592–1597

Endo M, Sugita T, Katsuda Y, Hidaka K, Sugiyama H (2010b) Programmed-assembly system using DNA jigsaw pieces. Chem Eur J 16:5362–5368

Eriksson T, Karlsson J, Tjerneld F (2002) A model explaining declining rate in hydrolysis of lignocellulose substrates with cellobiohydrolase I (*Cel*7A) and endoglucanase I (*Cel*7B) of Trichoderma reesei. Appl Biochem Biotechnol 101:41–60

Fantner GE, Barbero RJ, Gray DS, Belcher AM (2010) Kinetics of antimicrobial peptide activity measured on individual bacterial cells using high-speed atomic force microscopy. Nat Nanotechnol 5:280–285

Forgacs E, Cartwright S, Sakamoto T, Sellers JR, Corrie JET, Webb MR, White HD (2008) Kinetics of ADP dissociation from the trail and lead heads of actomyosin V following the power stroke. J Biol Chem 283:766–773

Forkey JN, Quinlan ME, Shaw MA, Corrie JET, Goldman YE (2003) Three-dimensional structural dynamics of myosin V by single-molecule fluorescence polarization. Nature 422:399–404

Fukuma T, Okazaki Y, Kodera N, Uchihashi T, Ando T (2008) High resonance frequency force microscope scanner using inertia balance support. Appl Phys Lett 92:243119 (3 pp)

Furuike S, Hossain MD, Maki Y, Adachi K, Suzuki T, Kohori A, Itoh H, Yoshida M, Kinosita K (2008) Axle-less F_1-ATPase rotates in the correct direction. Science 319:955–958

Geeves MA, Holmes KC (1999) Structura mechanism of muscle contraction. Annu Rev Biochem 68:687–728

Gilmore JL, Suzuki Y, Tamulaitis G, Siksnys V, Takeyasu K, Lyubchenko YL (2009) Single-molecule dynamics of the DNA-*EcoR*II protein complexes revealed with high-speed atomic force microscopy. Biochemistry 48:10492–10498

Giocondi M-C, Yamamoto D, Lesniewska E, Milhiet P-E, Ando T, Le Grimellec C (2010) Surface topography of membrane domains. Biochim Biophys Acta—Biomembranes 1798:703–718

Goldman YE (1987) Kinetics of the actomyosin ATPase in muscle fibers. Annu Rev Physiol 49:637–654

Guthold M, Bezanilla M, Erie DA, Jenkins B, Hansma HG, Bustamante C (1994) Following the assembly of RNA polymerase-DNA complexes in aqueous solutions with the scanning force microscope. Proc Natl Acad Sci USA 91:12927–12931

Häberle W, Hörber JKH, Ohnesorge F, Smith DPE, Binnig G (1992) In situ investigations of single living cells infected by viruses. Ultramicroscopy 42–44:1161–1167

Hansma HG, Bezanilla M, Zenhausern F, Adrian M, Sinsheimer RL (1993) Atomic force microscopy of DNA in aqueous solutions. Nucleic Acids Res 21:505–512

Henrissat B (1991) A classification of glycosyl hydrolases based on amino acid sequence similarities. Biochem J 280:309–316

Henrissat B, Bairoch A (1993) New families in the classification of glycosyl hydrolases based on amino acid sequence similarities. Biochem J 280:781–788

Henrissat B, Driguez H, Viet C, Schülein M (1985) Synergism of cellulases from Trichoderma reesei in the degradation of cellulose. Nat Biotechnol 3:722–726

Henrissat B, Teeri TT, Warren RA (1998) A scheme for designating enzymes that hydrolyse the polysaccharides in the cell walls of plants. FEBS Lett 425:352–354

Hon DNS (1994) Cellulose: a random walk along its historical path. Cellulose 1:1–25

Hossain MD, Furuike S, Maki Y, Adachi K, Ali MY, Huq M, Itoh H, Yoshida M, Kinosita K (2006) The rotor tip inside a bearing of a thermophilic F1-ATPase is dispensable for torque generation. Biophys J 90:4195–4203

Hossain MD, Furuike S, Maki Y, Adachi K, Suzuki T, Kohori A, Itoh H, Yoshida M, Kinosita K (2008) Neither helix in the coiled coil region of the axle of F1-ATPase plays a significant role in torque production. Biophys J 95:4837–4844

Hua W, Chung J, Gelles J (2002) Distinguishing inchworm and hand-over-hand processive kinesin movement by neck rotation measurements. Science 295:844–848

Huxley HE (1969) The mechanism of muscular contraction. Science 164:1356–1366

Igarashi K, Koivula A, Wada M, Kimura S, Penttilä M, Samejima M (2009) High speed atomic force microscopy visualizes processive movement of Trichoderma reesei cellobiohydrolase I on crystalline cellulose. J Biol Chem 284:36186–36190

Igarashi K, Uchihashi T, Koivula A, Wada M, Kimura S, Okamoto T, Penttila M, Ando T, Samejima M (2011) Traffic jams reduce hydrolytic efficiency of cellulase on cellulose surface. Science 333:1279–1282

Igarashi K, Wada M, Samejima M (2007) Activation of crystalline cellulose to cellulose III(I) results in efficient hydrolysis by cellobiohydrolase. FEBS J 274:1785–1792

Iko Y, Tabata KV, Sakakihara S, Nakashima T, Noji H (2009) Acceleration of the ATP-binding rate of F1-ATPase by forcible forward rotation. FEBS Lett 583:3187–3191

Imai T, Boisset C, Samejima M, Igarashi K, Sugiyama J (1998) Unidirectional processive action of cellobiohydrolase Cel7A on Valonia cellulose microcrystals. FEBS Lett 432:113–116

Inoue S, Uchihashi T, Yamamoto D, Ando T (2011) Direct observation of surfactant aggregate behavior on a mica surface using high-speed atomic force microscopy. Chem Commun 47:4974–4976

Itoh H, Takahashi A, Adachi K, Noji H, Yasuda R, Yoshida M, Kinosita K (2004) Mechanically driven ATP synthesis by F_1-ATPase. J Jpn Biochem Soc 427:42–45

Johansson G, Stahlberg J, Lindeberg G, Engstrom A, Pettersson G (1989) Isolated fungal cellulose terminal domains and a synthetic minimum analogue bind to cellulose. FEBS Lett 243:389–393

Joo C, Balci H, Ishitsuka Y, Buranachai C, Ha T (2008) Advances in single-molecule fluorescence methods for molecular biology. Annu Rev Biochem 77:51–76

Kaibara C, Matsui T, Hisabori T, Yoshida M (1996) Structural asymmetry of F_1-ATPase caused by the gamma subunit generates a high affinity nucleotide binding site. J Biol Chem 271:2433–2438

Kasas S, Thomson NH, Smith BL, Hansma HG, Zhu X, Guthold M, Bustamante C, Kool ET, Kashlev M, Hansma PK (1997) Escherichia coli RNA polymerase activity observed using atomic force microscopy. Biochemistry 36:461–468

Kitazawa M, Shiotani K, Toda A (2003) Batch fabrication of sharpened silicon nitride tips. Jpn J Appl Phys 42:4844–4847

Kodera N, Sakashita M, Ando T (2006) Dynamic proportional-integral-differential controller for high-speed atomic force microscopy. Rev Sci Instrum 77:083704 (7 pp)

Kodera N, Yamamoto D, Ishikawa R, Ando T (2010) Video imaging of walking myosin V by high-speed atomic force microscopy. Nature 468:72–76

Kodera N, Yamashita H, Ando T (2005) Active damping of the scanner for high-speed atomic force microscopy. Rev Sci Instrum 76:053708 (5 pp)

Kokavecz J, Tóth Z, Horváth ZL, Heszler P, Mechler Á (2006) Novel amplitude and frequency demodulation algorithm for a virtual dynamic atomic force microscope. Nanotechnology 17:S173–S177

De La Cruz EM, Wells AL, Rosenfeld SS, Ostap EM, Sweeney HL (1999) The kinetic mechanism of myosin V. Proc Natl Acad Sci USA 96:13726–13731

Lin H, Clegg DO, Lal R (1999) Imaging real-time proteolysis of single collagen I molecules with an atomic force microscope. Biochemistry 38:9956–9963

Linder M (1997) The roles and function of cellulose-binding domains. J Biotechnol 57:15–28

Lindsay SM, Nagahara LA, Thundat T, Knipping U, Rill RL, Drake B, Prater CB, Weisenhorn AL, Gould SA, Hansma PK (1989) STM and AFM images of nucleosome DNA under water. J Biomol Struct Dyn 7:279–287

Matsui T, Yoshida M (1995) Expression of the wild-type and the Cys-/Trp-less alpha 3 beta 3 gamma complex of thermophilic F_1-ATPase in *Escherichia coli*. Biochim Biophys 1231:139–146

Mehta AD, Rock RS, Rief M, Spudich JA, Mooseker MS, Cheney RE (1999) Myosin-V is a processive actin-based motor. Nature 400:590–593

Menz RI, Walker JE, Leslie AG (2001) Structure of bovine mitochondrial F(1)-ATPase with nucleotide bound to all three catalytic sites: implications for the mechanism of rotary catalysis. Cell 106:331–341

Milhiet P-E, Yamamoto D, Berthoumieu O, Dosset P, Le Grimellec C, Verdier J-M, Marchal S, Ando T (2010) Deciphering the structure, growth and assembly of amyloid-like fibrils using high-speed atomic force microscopy. PLoS One 5:e13240 (8 pp)

Miyagi A, Tsunaka Y, Uchihashi T, Mayanagi K, Hirose S, Morikawa K, Ando T (2008) Visualization of intrinsically disordered regions of proteins by high-speed atomic force microscopy. Chemphyschem 9:1859–1866

Müller DJ, Büldt G, Engel A (1995) Force-induced conformational change of bacteriorhodopsin. J Mol Biol 249:239–243

Müller DJ, Engel A (1999) Voltage and pH-induced channel closure of porin OmpF visualized by atomic force microscopy. J Mol Biol 285:1347–1351

Nakamoto RK, Ketchum CJ, Al-Shawi MK (1999) Rotational coupling in the F_0F_1 ATP synthase. Annu Rev Biophys Biomol Struct 28:205–234

Nidetzky B, Steiner W, Hayn M, Claeyssens M (1994) Cellulose hydrolysis by the cellulases from Trichoderma reesei: a new model for synergistic interaction. Biochem J 298:705–710

Nishiyama Y, Sugiyama J, Chanzy H, Langan P (2003) Crystal structure and hydrogen bonding system in cellulose I(alpha) from synchrotron X-ray and neutron fiber diffraction. J Am Chem Soc 125:14300–14306

Noji H, Yasuda R, Yoshida M, Kinosita K (1997) Direct observation of the rotation of F1-ATPase. Nature 386:299–302

Oberleithner H, Schillers H, Wilhelmi M, Butzke D, Danker T (2000) Nuclear pores collapse in response to CO2 imaged with atomic force microscopy. Pflugers Arch Eur J Physiol 439:251–255

Oguchi Y, Mikhailenko SV, Ohki T, Olivares AO, De La Cruz EM, Ishiwata S (2008) Load-dependent ADP binding to myosins V and VI: implications for subunit coordination and function. Proc Natl Acad Sci USA 105:7714–7719

Ohnesorge F, Heckl WM, Häberle W, Pum D, Sara M, Schindler H, Schilcher K, Kiener A, Smith DP, Sleytr UB (1992) Scanning force microscopy studies of the S-layers from Bacillus coagulans E38-66, Bacillus sphaericus CCM2177 and of an antibody binding process. Ultramicroscopy 42–44:1236–1242

Okada T, Tanaka H, Iwane AH, Kitamura K, Ikebe M, Yanagida T (2007) The diffusive search mechanism of processive myosin class-V motor involves directional steps along actin subunits. Biochem Biophys Res Commun 354:379–384

Oke OA, Burgess SA, Forgacs E, Knight PJ, Sakamoto T, Sellers JR, White H, Trinick J (2010) Influence of lever structure on myosin 5a walking. Proc Natl Acad Sci USA 107:2509–2514

Peterman EJG, Sosa H, Moerner WE (2004) Single-molecule fluorescence spectroscopy and microscopy of biomolecular motors. Annu Rev Phys Chem 55:79–96

Purcell TJ, Sweeney HL, Spudich JA (2005) A force-dependent state controls the coordination of processive myosin V. Proc Natl Acad Sci USA 102:13873–13878

Putman CAJ, Van Der Werf KO, De Grooth BG, Van Hulst NF, Greve J (1994) Tapping mode atomic force microscopy in liquid. Appl Phys Lett 64:2454–2456

Rajendran A, Endo M, Katsuda Y, Hidaka K, Sugiyama H (2011) Programmed two-dimensional self-assembly of multiple DNA origami jigsaw pieces. ACS Nano 5:665–671

Reverbel-Leroy C, Pages S, Belaich A, Belaich JP, Tardif C (1997) The processive endocellulase CelF, a major component of the Clostridium cellulolyticum cellulosome: purification and characterization of the recombinant form. J Bacteriol 179:46–52

Rondelez Y, Tresset G, Nakashima T, Kato-Yamada Y, Fujita H, Takeuchi S, Noji H (2005) Highly coupled ATP synthesis by F_1-ATPase single molecules. Nature 433:773–777

Rosenfeld SS, Sweeney HL (2004) A model of myosin V processivity. J Biol Chem 279:40100–40111

Rouvinen J, Bergfors T, Teeri T, Knowles JK, Jones TA (1990) Three-dimensional structure of cellobiohydrolase II from *Trichoderma reesei*. Science 249:380–386

Roy R, Hohng S, Ha T (2008) A practical guide to single-molecule FRET. Nat Methods 5:507–516

Ryu DDY, Mandels M (1980) Cellulases: biosynthesis and applications. Enzyme Microb Technol 2:91–102

Sakamoto T, Amitani I, Yokota E, Ando T (2000) Direct observation of processive movement by individual myosin V molecules. Biochem Biophys Res Commun 272:586–590

Sakamoto T, Webb MR, Forgacs E, White HD, Sellers JR (2008) Direct observation of the mechanochemical coupling in myosin Va during processive movement. Nature 455:128–132

Sannohe Y, Endo M, Katsuda Y, Hidaka K, Sugiyama H (2010) Visualization of dynamic conformational switching of the G-quadruplex in a DNA nanostructure. J Am Chem Soc 132:16311–16313

Schabert FA, Engel A (1994) Reproducible acquisition of *Escherichia coli* porin surface topographs by atomic force microscopy. Biophys J 67:2394–2403

Schäffer TE, Cleveland JP, Ohnesorge F, Walters DA, Hansma PK (1996) Studies of vibrating atomic force microscope cantilevers in liquid. J Appl Phys 80:3622–3627

Sellers JR, Weisman LS (2008) Myosins: a superfamily of molecular motors. In: Coluccio LM (ed) Proteins and cell regulation. Springer, Netherland, pp 289–324

Shao Z, Yang J (1995) Progress in high resolution atomic force microscopy in biology. Q Rev Biophys 28:195–251

Shibata M, Uchihashi T, Yamashita H, Kandori H, Ando T (2011) Structural changes in bacterio-rhodopsin in response to alternate illumination observed by high-speed atomic force microscopy. Angew Chem Int Ed 50:4410–4413

Shibata M, Yamashita H, Uchihashi T, Kandori H, Ando T (2010) High-speed atomic force microscopy shows dynamic molecular processes in photoactivated bacteriorhodopsin. Nat Nanotechnol 5:208–212

Shinozaki Y, Sumitomo K, Tsuda M, Koizumi S, Inoue K, Torimitsu K (2009) Direct observation of ATP-induced conformational changes in single P2X4 receptors. PLoS Biol 7:e1000103 (12 pp)

Shirakihara Y, Leslie AG, Abrahams JP, Walker JE, Ueda T, Sekimoto Y, Kambara M, Saika K, Kagawa Y, Yoshida M (1997) The crystal structure of the nucleotide-free alpha 3 beta 3 subcomplex of F1-ATPase from the thermophilic Bacillus PS3 is a symmetric trimer. Structure 5:825–836

Ståhlberg J, Johansson G, Pettersson G (1991) A new model for enzymatic hydrolysis of cellulose based on the two-domain structure of cellobiohydrolase I. Bio/Technology 9:286–290

Sugimoto S, Yamanaka K, Nishikori S, Miyagi A, Ando T, Ogura T (2010) AAA+ chaperone ClpX regulates dynamics of prokaryotic cytoskeletal protein FtsZ. J Biol Chem 285:6648–6657

Suzuki Y, Higuchi Y, Hizume K, Yokokawa M, Yoshimura SH, Yoshikawa K, Takeyasu K (2010) Molecular dynamics of DNA and nucleosomes in solution studied by fast-scanning atomic force microscopy. Ultramicroscopy 110:682–688

Teeri TT (1997) Crystalline cellulose degradation: new insight into the function of cellobiohydrolases. Trends Biotechnol 15:160–167

Teeri TT, Koivula A, Linder M, Wohlfahrt G, Divne C, Jones TA (1998) Trichoderma reesei cellobiohydrolases: why so efficient on crystalline cellulose? Biochem Soc Trans 26:173–178

Todd RD, Griesenbeck TA, Douglas MG (1980) The yeast mitochondrial adenosine triphosphatase complex Subunit stoichiometry and physical characterization. J Biol Chem 255:5461–5467

Uchihashi T, Iino R, Ando T, Noji H (2011) High-speed atomic force microscopy reveals rotary catalysis of rotorless F_1-ATPase. Science 333:755–758

Veigel C, Schmitz S, Wang F, Sellers JR (2005) Load-dependent kinetics of myosin-V can explain its high processivity. Nat Cell Biol 7:861–869

Vianni MB, Pietrasanta LI, Thompson JB, Chand A, Gebeshuber IC, Kindt JH, Richter M, Hansma HG, Hansma PK (2000) Probing protein-proein interactions in real time. Nature Struct Biol 7:644–647

Wada M, Chanzy H, Nishiyama Y, Langan P (2004) Cellulose III I crystal structure and hydrogen bonding by synchrotron X-ray and neutron fiber diffraction. Macromolecules 37:8548–8555

Walker JE, Fearnley IM, Gay NJ, Gibson BW, Northrop FD, Powell SJ, Runswick MJ, Saraste M, Tybulewicz VL (1985) Primary structure and subunit stoichiometry of F1-ATPase from bovine mitochondria. J Mol Biol 184:677–701

Walker ML, Burgess SA, Sellers JR, Wang F, Hammer JA, Trinick J, Knight PJ (2000) Two-headed binding of a processive myosin to F-actin. Nature 405:804–807

Walz T, Tittmann P, Fuchs KH, Müller DJ, Smith BL, Agre P, Gross H, Engel A (1996) Surface topographies at subnanometer-resolution reveal asymmetry and sidedness of aquaporin-1. J Mol Biol 264:907–918

Wang H, Oster G (1998) Energy transduction in the F1 motor of ATP synthase. Nature 396:279–282

Watanabe R, Iino R, Noji H (2010) Phosphate release in F1-ATPase catalytic cycle follows ADP release. Nat Chem Biol 6:814–820

Weisenhorn AL, Hansma PK, Albrecht TR, Quate CF (1989) Forces in atomic force microscopy in air and water. Appl Phys Lett 54:2651 (3 pp)

Wendel M, Lorenz H, Kotthaus JP (1995) Sharpened electron beam deposited tips for high resolution atomic force microscope lithography and imaging. Appl Phys Lett 67:3732 (3 pp)

Wickham SFJ, Endo M, Katsuda Y, Hidaka K, Bath J, Sugiyama H, Turberfield AJ (2011) Direct observation of stepwise movement of a synthetic molecular transporter. Nat Nanotechnol 6:166–169

Wood TM, McCrae SI (1978) The cellulase of Trichoderma koningii purification and properties of some endoglucanase components with special reference to their action on cellulose when acting alone and in synergism with the cellobiohydrolase. Biochem J 171:61–72

Yamamoto D, Nagura N, Omote S, Taniguchi M, Ando T (2009) Streptavidin 2D crystal substrates for visualizing biomolecular processes by atomic force microscopy. Biophys J 97:2358–2367

Yamamoto D, Uchihashi T, Kodera N, Ando T (2008) Anisotropic diffusion of point defects in a two-dimensional crystal of streptavidin observed by high-speed atomic force microscopy. Nanotechnology 19:384009 (9 pp)

Yamamoto D, Uchihashi T, Kodera N, Yamashita H, Nishikori S, Ogura T, Shibata M, Ando T (2010) High-speed atomic force microscopy techniques for observing dynamic biomolecular processes. Methods Enzymol 475:541–564

Yamashita H, Voïtchovsky K, Uchihashi T, Contera SA, Ryan JF, Ando T (2009) Dynamics of bacteriorhodopsin 2D crystal observed by high-speed atomic force microscopy. J Struct Biol 167:153–158

Yanagida T, Ishii Y (eds) (2008) Single molecule dynamics in life science. Wiley, Weinheim

Yasuda R, Noji H, Kinosita K, Yoshida M (1998) F_1-ATPase is a highly efficient molecular motor that rotates with discrete 120 degree steps. Cell 93:1117–1124

Yildiz A, Forkey JN, McKinney SA, Ha T, Goldman YE, Selvin PR (2003) Myosin V walks hand-over-hand: single fluorophore imaging with 1.5-nm localization. Science 300:2061–2065

Yokokawa M, Carnally SM, Henderson RM, Takeyasu K, Edwardson JM (2010) Acid-sensing ion channel (ASIC) 1a undergoes a height transition in response to acidification. FEBS Lett 584:3107–3110

Yokokawa M, Wada C, Ando T, Sakai N, Yagi A, Yoshimura SH, Takeyasu K (2006a) Fast-scanning atomic force microscopy reveals the ATP/ADP-dependent conformational changes of GroEL. EMBO J 25:4567–4576

Yokokawa M, Yoshimura SH, Naito Y, Ando T, Yagi A, Sakai N, Takeyasu K (2006b) Fast-scanning atomic force microscopy reveals the molecular mechanism of DNA cleavage by ApaI endonuclease. IEE Proc Nanobiotechnol 153:60–66

Yoshida M, Allison WS (1990) The ATPase activity of the alpha 3 beta 3 complex of the F_1-ATPase of the thermophilic bacterium PS_3 is inactivated on modification of tyrosine 307 in a single beta subunit by 7-chloro-4-nitrobenzofurazan. J Biol Chem 265:2483–2487

Zhong Q, Inniss D, Kjoller K, Elings VB (1993) Fractured polymer/silica fiber surface studied by tapping mode atomic force. Surf Sci Lett 290:L688–L692